Earth and Planetary Science Letters
January 2023, Volume 601 Pages 117910 (10p.)
https://doi.org/10.1016/j.epsl.2022.117910
https://archimer.ifremer.fr/doc/00805/91715/

Hafnium isotope evidence for enhanced weatherability at high southern latitudes during Oceanic Anoxic Event 2

Chen Hongjin [1, 2, 6], Bayon Germain [2],, * Xu Zhaokai [1, 3, 4, 5, *], Li Tiegang [6]

[1] CAS Key Laboratory of Marine Geology and Environment, Institute of Oceanology, Chinese Academy of Sciences, Qingdao 266071, China
[2] Univ. Brest, CNRS, Ifremer, Geo-Ocean, F-29280 Plouzané, France
[3] Laboratory for Marine Geology, Pilot National Laboratory for Marine Science and Technology (Qingdao), Qingdao 266061, China
[4] CAS Center for Excellence in Quaternary Science and Global Change, Xi'an 710061, China
[5] Center for Ocean Mega-Science, Chinese Academy of Sciences, Qingdao 266071, China
[6] Key Laboratory of Marine Mineral Resources, Ministry of Natural Resources, Guangzhou Marine Geological Survey, China Geological Survey, Guangzhou 510075, China
[7] Key Laboratory of Marine Sedimentology and Metallogeny, First Institute of Oceanography, Ministry of Natural Resources, Qingdao 266061, China

* Corresponding authors : Germain Bayon, email address : Germain.Bayon@ifremer.fr ; Zhaokai Xu, email address : zhaokaixu@qdio.ac.cn

Abstract :

The Oceanic Anoxic Event 2 (OAE 2; ca. ~94 Ma) represents one of the most extreme carbon cycle perturbations of the Phanerozoic, which coincided with major environmental and climate reorganization in both terrestrial and marine realms. Chemical weathering of continental silicate rocks is thought to have played a crucial role during OAE 2, through enhanced release of bio-essential nutrients to the ocean, promoting high rates of marine primary production and organic carbon burial, but also due to its effect on atmospheric CO2 drawdown, which altogether possibly drove the OAE 2 termination. Yet, the evolution of continental chemical weathering during OAE 2 remains poorly defined, especially in high-latitude regions. In this study, we present a combined hafnium-neodymium isotope investigation of the clay-size detrital fraction (△εHfclay) of late Cenomanian to early Turonian sediments from the southwest Australian margin, at a site (International Ocean Discovery Program U1516) located in the southern high latitudes (~62°S) during the late Cretaceous. The reliability of △εHfclay as a proxy for continental chemical weathering in ancient anoxic marine sediments was assessed by analyzing a suite of samples retrieved from methanogenic sediments experiencing marine silicate weathering at ocean margins, suggesting negligible effect of reverse weathering on hafnium-neodymium isotope compositions. At Site U1516, the early stage of OAE 2 was characterized by relatively low △εHfclay values (−5.9 ± 2), typical of reduced chemical weathering in nearby continental regions. At the onset of the most prominent carbon isotope excursion, an abrupt decrease in △εHfclay points towards accelerated export of poorly weathered sediments resulting from the abrupt reactivation of river systems in southwest Australia. This period was followed by a pronounced △εHfclay shift towards positive values, indicative of intensifying chemical weathering conditions during the OAE 2 interval showing the highest C anomaly. Based on these results, we posit that enhanced hydrological cycle, most likely caused by a southward shift of the westerlies, led to a large increase in weatherability at southern high latitudes during peak OAE 2 warmth. This finding

provides empirical support for the potential role played by high-latitude weathering systems in driving the termination of OAE 2, via weathering-driven consumption of atmospheric CO2 and accelerated riverine fluxes of nutrients leading to enhanced organic carbon burial in marine sediments.

Highlights

► Combined Nd-Hf isotopes as a proxy for continental weathering during OAE 2. ► Negligible influence of reverse weathering on Hf-Nd isotopes in marine clays. ► Intensifying weathering and river discharge in SW Australia during peak OAE 2 warmth. ► Southward shift of westerlies drove enhanced weatherability in southern high-latitude regions.

Keywords : OAE 2, IODP expedition 369, Mentelle Basin, hafnium-neodymium isotopes, silicate weathering, reverse weathering

1. Introduction

Understanding the dynamics of the Earth's climate system during past carbon cycle perturbations is essential to improve predictions on future climate change (Huber et al., 2019; Takashima et al., 2006). The Oceanic Anoxic Event 2 (OAE 2), which occurred at the Cenomanian-Turonian boundary (~94.5 to 93.9 Ma), represents the most significant global carbon cycle perturbation of the Late Cretaceous (Arthur et al., 1987; Schlanger and Jenkyns, 1976), characterized by widespread organic carbon sequestration and a pronounced positive carbon isotope excursion (CIE, ~2‰) in the sedimentary record (Jenkyns, 2010; Tsikos et al., 2004). Possible driving mechanisms for OAE 2 have long been debated, but consensus exists that it was closely related to the emplacement of large igneous provinces (LIP) at that time (Fig. 1) (e.g., Turgeon and Creaser, 2008), associated with massive CO_2 release into the atmosphere (O'Brien et al., 2017), enhanced hydrological cycle (van Helmond et al., 2013) and increased marine primary production (Schlanger and Jenkyns, 1976). Following emplacement of LIPs, sustained chemical weathering of freshly exposed mafic rocks under warm and wet conditions most likely represented a major sink for atmospheric CO_2 (e.g., Macdonald et al., 2019), possibly playing a role in the OAE 2 termination and the recovery of the Earth's climate system from greenhouse conditions (e.g., Pogge von Strandmann et al., 2013). Additionally, enhanced global 'weatherability'; a term that refers to the ease with which terrestrial rocks are subject to chemical weathering at the Earth's surface, and implicitly relates to riverine solute fluxes (e.g., Kump et al., 2000; Mills et al., 2014; Penman et al., 2020), presumably resulted in accelerated continental

fluxes of phosphate and other key nutrients to the oceans, thereby contributing to high rates of primary productivity and organic carbon burial (e.g., Jenkyns, 2010; Pogge von Strandmann et al., 2013; Yobo et al., 2021). Up to now, the evolution of continental chemical weathering during OAE 2 and other past global carbon cycle perturbations of the Phanerozoic has been mostly inferred from the application of isotope proxies (e.g., Li, Ca, Sr, and Os) to the sedimentary record of ancient seawater chemistry (Blättler et al., 2011; Bottini et al., 2012; Frijia and Parente, 2008; Pogge von Strandmann et al., 2013). Changes in continental chemical weathering fluxes during the OAE 2 have been documented at a very few locations in the Northern Hemisphere, using Li isotopes in the carbonate record as a proxy for global seawater chemistry (Pogge von Strandmann et al., 2013). Unlike other marine-based proxies, the δ^7Li composition of marine carbonate mostly reflects the global continental flux and isotopic composition of dissolved riverine Li related to chemical weathering of silicate rocks (Misra and Froelich, 2012; Pogge von Strandmann et al., 2013). However, the lack of additional proxy evidence at the regional scale, especially for high-latitude regions, still hampers our understanding of the way continental chemical weathering may have responded to rapid climate change during the OAE 2, and whether chemical weathering contributed to driving the termination of greenhouse climate state.

The combined use of hafnium (Hf) and neodymium (Nd) isotope ratios in the clay-size fraction of siliciclastic sediments represents a novel promising approach for reconstructing regional changes in past continental weathering (Bayon et al., 2022;

Corentin et al., 2022). Most igneous rocks and terrestrial sediments lie along a single correlation trend in a $^{143}Nd/^{144}Nd$ (or ε_{Nd} in epsilon notation) versus $^{176}Hf/^{177}Hf$ (ε_{Hf}) plot, defined as the 'Terrestrial Array' ($\varepsilon_{Hf} = 1.55 \times \varepsilon_{Nd} + 1.21$) (Fig. 2) (Vervoort et al., 2011). While the Nd isotopic composition of fine-grained detrital sediments remains mostly unchanged during continental erosion, sediment transport and deposition (e.g., Bayon et al., 2015), Hf isotopes are strongly affected by preferential sorting of Hf-bearing zircon into coarse sediments during transport processes (e.g., Bayon et al., 2009; Garçon et al., 2013). Because zircons are typically characterized by unradiogenic signatures (with low ε_{Hf}) and dominate the Hf budget in detrital sediments, sediment transport hence results in zircon-depleted clay-size sediment fractions exhibiting much higher ε_{Hf} composition than corresponding zircon-bearing silts, defining a so-called 'Clay Array' in the ε_{Nd} versus ε_{Hf} plot ($\varepsilon_{Hf} = 0.78 \times \varepsilon_{Nd} + 5.23$; Zhao et al., 2014; Bayon et al., 2016). In addition to the 'zircon effect', preferential dissolution of accessory Lu-rich minerals such as apatite during continental chemical weathering releases substantial amounts of radiogenic Hf to surface environments (e.g., Bayon et al., 2006; Rickli et al., 2013). This process most likely explains why seawater and river waters typically display radiogenic (high) ε_{Hf} composition relative to ε_{Nd} (Fig. 2) (e.g., Bayon et al., 2006; Rickli et al., 2013). Bayon et al. (2016) showed that the decoupling of Hf and Nd isotopes during continental weathering is also recorded in the clay-size fraction of river-borne sediments, demonstrating strong relationships with environmental parameters and the intensity of chemical weathering. The degree of Hf-Nd isotope decoupling during chemical weathering can be quantitatively measured using the

vertical ε_{Hf} deviation from the 'Clay Array' (Bayon et al., 2016). This index, termed $\triangle\varepsilon_{Hfclay}$, can serve as a unique proxy for reconstructing continental weathering and past environmental conditions over various geological timescales (e.g., Bayon et al., 2022; Corentin et al., 2022). However, to date, whether this proxy can be successfully applied to sediments or sedimentary rocks that have experienced intense post-depositional processes such as reverse weathering and clay authigenesis still remains unclear (Bayon et al., 2022).

In this study, we present Hf and Nd isotopic compositions and elemental geochemistry of clay-size (<2 μm) siliciclastic fractions of fine-grained sediments deposited at the International Ocean Discovery Program (IODP) Site U1516 during OAE 2 (Fig. 1), combined with additional Hf-Nd isotope analyses of clays extracted from methanogenic sediments strongly influenced by marine silicate weathering (i.e., reverse weathering). This study aims to examine the potential impact of reverse weathering on $\triangle\varepsilon_{Hfclay}$ and its utility as a weathering proxy, and to investigate how chemical weathering in southern high latitudes may have responded to greenhouse climate change during OAE 2.

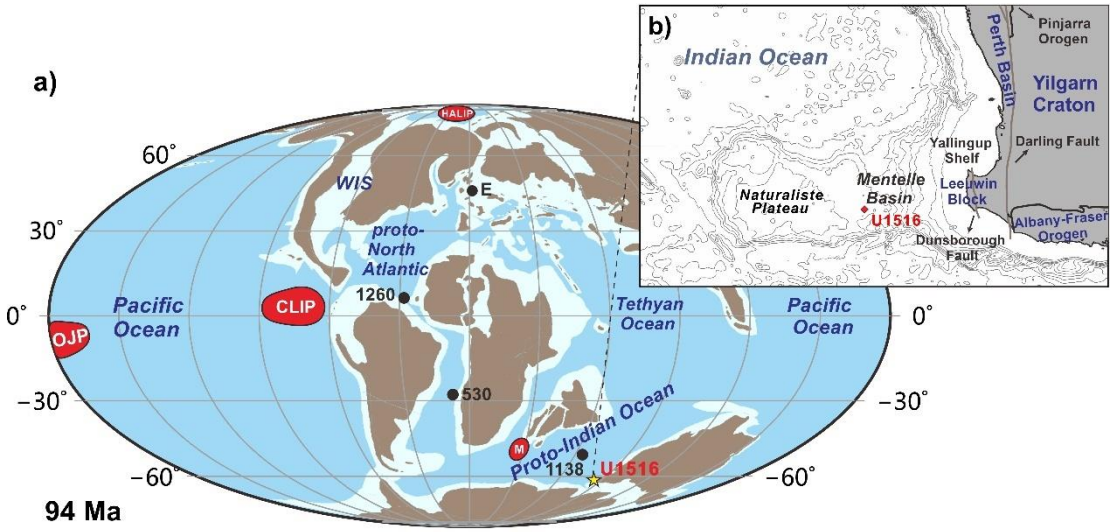

Fig. 1. a) Paleogeographic map of ~94 Ma showing IODP site U1516 in this study and reference sites from previous studies (Dickson et al., 2017; Du Vivier et al., 2015; Pogge von Strandmann et al., 2013); b) Modern regional context of the Mentelle Basin, Naturaliste Plateau, and southwest Australia showing the location of Site U1516 and the potential sediment sources of southwest Australia. E, Eastbourne, UK; WIS, Western Interior Basin; 1260, Ocean Drilling Program (ODP) Site 1260, Demerara Rise; 530, Deep Sea Drilling Project Site 530, Angola Basin; 1138, ODP Site 1138, Kerguelen Plateau. The High Arctic, Caribbean, Ontong-Java, and Madagascar LIPs are marked as HALIP, CLIP, OJP and M, respectively. Modified from Du Vivier et al. (2015).

2. Materials

Site U1516 (34° 20.92′S, 112° 47.96′E; water depth ~2675 m) was drilled in the Mentelle Basin off southwest Australia during the IODP Expedition 369 (Fig. 1), recovering a sedimentary record from the Albian to Pleistocene (Huber et al., 2019). In this study, we mainly focus on the interval between 473.94 and 460.13 m revised core composited sea floor (rCCSF), which corresponds to the late Cenomanian to early

Turonian interval. At Site U1516, the OAE 2 interval was identified between 473.94 and 466.30 rCCSF based on both stratigraphic correlation of the U1516 $\delta^{13}C$ record with the reference section at Eastbourne (UK) and nannofossil-foraminiferal biostratigraphy (Petrizzo et al., 2021; Tsikos et al., 2004). Note that the stratigraphic position of the OAE 2 interval in this study has been slightly revised from Petrizzo et al. (2021), in order to take into account the presence of a major carbonate dissolution event (e.g., Chen et al., 2022) and the possible diachrony of nannofossil datums at Site U1516 (e.g., Boulila et al., 2020). Yet, additional work based on astronomical tuning will be required to further refine the age model around the OAE 2 interval (Batenburg et al., 2021). The estimated duration of OAE 2 at Site U1516 is ~800 kyr based on the age-depth model established by Petrizzo et al. (2021), which is in agreement with estimates for other stratigraphic sections at high southern latitudes (e.g., Gangl et al., 2019). At Site U1516, the OAE 2 is characterized by the occurrence of a carbonate-poor interval between 467.37 and 470.12 m rCCSF, accompanied by the deposition of a black (organic-rich) shale unit at ~470 m rCCSF (Petrizzo et al., 2021). The rest of the OAE 2 interval is composed of claystone, clayey nannofossil chalk, and calcareous/nannofossil chalk with clay interbedded with chert (Huber et al., 2019). Thirty-five samples from Site U1516 were analyzed in this study. The OAE 2 interval at Site U1516 was split into two main sediment intervals based on sediment provenance, which correspond to the so-called Phase I (between 473.94 and 471.40 m rCCSF) and Phase II (471.40–466.30 m rCCSF) (Fig. 3; Chen et al., 2022). Phase II corresponds to the most prominent CIE associated with a major provenance change inferred from Nd

isotopes, interpreted as reflecting enhanced hydrological cycle in southwest Australia (Chen et al., 2022). Note that the Plenus Cold Event (PCE); an episode of transient cooling during OAE 2 previously identified at several Northern Hemisphere sites (e.g., O'Connor et al., 2020), possibly correlates to the interval between 472.54 and 470.72 m rCCSF at Site U1516, although direct proxy evidence for significant cooling during PCE is yet to be found (Petrizzo et al., 2021).

In order to constrain the potential influence of post-depositional alteration and clay authigenesis (i.e., reverse weathering) on measured Hf isotopic compositions, a suite of sediment samples (n=20) was analyzed from various ODP and IODP sites (n=10) at ocean margins worldwide (Angola margin, Congo Fan, Peru Trench, Chile margin, Hydrate Ridge, Bering Sea, and Papua New Guinea margin). These sites are characterized by high inputs of lithogenic and organic matter, experiencing intense early diagenetic processes that result in methanogenesis, marine silicate weathering under anoxic conditions, and presumably clay authigenesis (Table S1). For each site, sediment samples associated with both low and high total alkalinity (TA) values in pore waters (up to 160 mM; obtained from shipboard data; see Supplementary Information Table S1 and references therein) were analyzed for comparison. Note that high total alkalinity values (TA > ~40 mM) in pore waters are generally taken as indicative of marine silicate weathering (Wallmann et al., 2008).

3. Methods

Both Hf and Nd isotopic compositions were conducted on clay-size siliciclastic fractions. Prior to analyses, carbonate, Fe-Mn oxyhydroxide phases and organic matter were removed from the bulk sediment using a sequential leaching procedure, followed by separation of clay-size (<2 μm) detrital fractions using low-speed centrifugation (Bayon et al., 2015; Bayon et al., 2022). Note that all Nd isotope data for the same Site U1516 samples used in this study have been reported in a companion paper focused on sediment provenance (Chen et al., 2022), in which all details on sample preparation and digestion can be found.

The abundances of selected major and trace elements in clay-size fractions were determined at the Pôle Spectrométrie Océan (Brest) using a Thermo Scientific Element XR sector field ICP-MS. The precision for major and trace elements was better than 3% and 5%, respectively. The accuracy of our data was assessed by analyzing five geological-certified reference materials (BHVO-2, AGV-1, BCR-1, DNC-1, and UB-N). The results obtained for the reference materials gave an accuracy typically better than 8%.

Hafnium and neodymium were purified by ion exchange chromatography (Bayon et al., 2016), and Hf-Nd isotopic measurements were conducted at the Pôle Spectrométrie Océan (Brest) using a Thermo Scientific Neptune multi-collector ICP-MS. Hf and Nd isotopic compositions were determined using sample-standard bracketing, by analyzing AMES and Nd Spex standard solutions every two samples, respectively. All measured

Hf and Nd isotopic ratios were corrected from mass bias using $^{179}Hf/^{177}Hf = 0.7325$ and $^{146}Nd/^{144}Nd = 0.7129$, respectively. During analytical sessions, Hf and Nd isotopic compositions of JMC-475 and JNdi-1 solutions yielded 0.282162 ± 0.000004 (2 SD; n=12) and 0.512116 ± 0.000005 (2 SD; n=8) values similar to reference values. Hf and Nd isotopic ratios are expressed using the epsilon notation, with $\varepsilon_{Hf} = [(^{176}Hf/^{177}Hf)_{sample} / (^{176}Hf/^{177}Hf)_{CHUR} - 1] \times 10000$ and $\varepsilon_{Nd} = [(^{143}Nd/^{144}Nd)_{sample} / (^{143}Nd/^{144}Nd)_{CHUR} - 1] \times 10000$; using Chondritic Uniform Reservoir (CHUR) values of 0.282785 and 0.512630 for Hf and Nd isotopic ratios, respectively (Bouvier et al., 2008). Initial $\varepsilon_{Nd(i)}$ and $\varepsilon_{Hf(i)}$ values were calculated using elemental Sm/Nd and Lu/Hf ratios (see details in Bayon et al., 2022) and stratigraphic ages provided by the age model (Petrizzo et al., 2021).

4. Results

4.1 Nd-Hf isotopic compositions of clay-size fractions at Site U1516

Hafnium isotope ratios for clay-size siliciclastic fractions at Site U1516 are reported in Table 1, together with recently published Nd isotope data for the same samples (Chen et al., 2022). Corresponding major and trace element data are listed in the supplementary dataset.

Note that three samples of clay-size fraction exhibiting anomalous shale-normalized rare earth element (REE) patterns, indicating the presence of residual authigenic phases or accessory heavy minerals, were discarded for the discussion based on Nd-Hf isotopes (see Supplementary text; Fig. S1). All clay-size fractions at Site U1516 show negative

$\varepsilon_{Hf(i)}$ values, ranging between -18.2 and -7.7 (Table 1), and plot between the correlation trends defined by the Clay Array and the Terrestrial Array (Fig. 2). The vertical deviation of measured Hf isotopic compositions relative to the Clay Array yields $\triangle\varepsilon_{Hfclay}$ values ranging between -11.5 and +1.8 (Table 1 and Fig. 2). Unlike Nd isotopes, which displayed a shift towards unradiogenic values (from -11.1 to 23.2) during Phase II of the OAE 2 (Fig. 2) (Chen et al., 2022), $\varepsilon_{Hf(i)}$ values exhibit relatively smaller variability across the OAE 2 (between -14.9 and -7.7), except for a prominent shift towards highly negative values (down to ~ -18.2) within the black shale unit (Fig. 2). The degree of Hf-Nd isotope decoupling in clay-size fractions ($\triangle\varepsilon_{Hfclay}$) displays two major changes at Site U1516: a first shift from ~-5.9 to ~-11.5 at the beginning of Phase II of the OAE 2, with the lowest values coincident with black shale deposition, followed by a major shift towards positive $\triangle\varepsilon_{Hfclay}$ values between 470.26 and 468.84 m rCCSF (Fig. 2).

4.2 Hf and Nd isotopes in methanogenic sediments

Clay-size fractions separated from methanogenic sediments experiencing marine silicate weathering at ocean margins display a large range of Hf and Nd isotopic compositions (Fig. 2 and Table S1), from unradiogenic values typical of passive continental margin settings (Black Ridge, Angola margin and Congo Fan) to radiogenic values at active ocean margins (Peru trench, Chile margin, Hydrate Ridge, Bering Sea and Papua New Guinea margin). At each site, clay-size fractions extracted from sediment layers associated with both low and high TA values in pore waters display

similar $\varepsilon_{Nd(i)}$ and $\varepsilon_{Hf(i)}$ values (Fig. 2 and Table S1), plotting near the Clay Array and the field of volcanogenic river clays (Bayon et al., 2016), thus yielding near-zero $\triangle\varepsilon_{Hfclay}$ values.

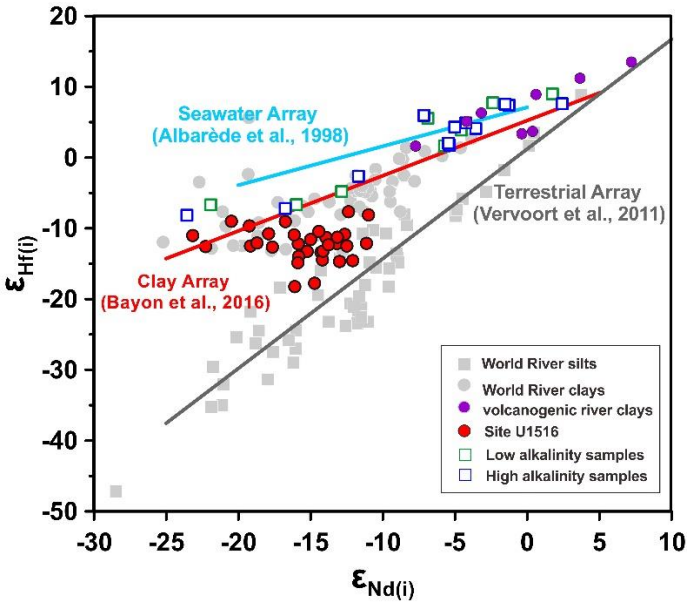

Fig. 2. Hf and Nd isotopic compositions of clay-size fractions of Site U1516 (red circles) and other continental margin sediments recovered from low- and high-alkalinity pore-water environments. Data for modern river clays and silts worldwide are shown for comparison (Bayon et al., 2016; Bayon et al., 2022), together with the present-day Terrestrial Array ($\varepsilon_{Hf} = 1.55 \times \varepsilon_{Nd} + 1.21$; dark grey line; Vervoort et al., 2011), the Clay Array ($\varepsilon_{Hf} = 0.78 \times \varepsilon_{Nd} + 5.23$; red line; Bayon et al., 2016), and the Seawater Array ($\varepsilon_{Hf} = 0.55 \times \varepsilon_{Nd} + 7.1$; blue line; Albarède et al., 1998). Green squares refer to clay-size fractions separated from continental margin sediments associated with pore waters displaying low-alkalinity (seawater-like) values, while blue squares correspond to samples with high-alkalinity pore water levels, indicative of anoxic silicate weathering.

1

2

3

Table 1 Hf and Nd isotopic composition of the clay-size fraction of OAE 2 sediments at IODP Site U1516.

Sample ID	Hole	Core	Type	Section	Top offset (cm)	Bottom offset (cm)	rCCSF (m)	$^{176}Hf/^{177}Hf$ ± 2 se	$^{143}Nd/^{144}Nd$ ± 2 se*	$\varepsilon_{Hf(i)}$	$\varepsilon_{Nd(i)}$	$\triangle\varepsilon_{Hfclay}$
M1	D	2	R	3	8	9	460.28	0.282442 ± 9	0.5118026 ± 4	-10.6	-15.2	-4.0
M2	C	30	R	2	50	51	461.22	0.282342 ± 9	0.5119581 ± 3	-14.6	-12.1	-10.4
M3	D	3	R	2	71	72	464.96	0.282437 ± 9	0.5118602 ± 4	-11.3	-13.9	-5.6
M4	C	31	R	2	27	28	465.99	0.282355 ± 8	0.5119102 ± 3	-14.7	-13.0	-9.8
M5	C	31	R	2	60	61	466.32	0.282483 ± 9	0.5119989 ± 2	-11.8	-11.4	-8.2
M6	C	31	R	2	95	96	466.67	0.282394 ± 7	0.5118602 ± 3	-13.4	-14.3	-7.5
M7	C	31	R	3	35	36	467.34	0.282444 ± 7	0.5118125 ± 3	-11.6	-15.0	-5.1
M8	D	4	R	1	95	97	467.95	0.282388 ± 7	0.5117960 ± 4	-13.3	-15.2	-6.6
M9	D	4	R	1	125	127	468.25	0.282398 ± 8	0.5115885 ± 5	-12.5	-19.2	-2.8
M10	D	4	R	2	22	24	468.51	0.282397 ± 7	0.5114325 ± 6	-12.6	-22.3	-0.4
M11	D	4	R	2	55	57	468.84	0.282489 ± 8	0.5115904 ± 3	-9.7	-19.2	0.1
M12	D	4	R	2	86	88	469.15	0.282507 ± 6	0.5117217 ± 4	-9.1	-16.7	-1.2
M13	D	4	R	3	1	3	469.44	0.282495 ± 7	0.5115217 ± 4	-9.0	-20.5	1.7
M14	D	4	R	3	15	16	469.57	0.282435 ± 6	0.5113823 ± 4	-11.0	-23.2	1.8
M15	D	4	R	3	47	49	469.90	0.282407 ± 7	0.5117544 ± 4	-12.2	-15.9	-5.1
M16	D	4	R	3	51	52	469.94	0.282399 ± 6	0.5116689 ± 3	-12.6	-17.6	-4.1
M17	D	4	R	3	55	56	469.98	0.282453 ± 8	0.5117427 ± 4	-10.9	-16.1	-3.6
M18	D	4	R	3	59	60	470.02	0.282407 ± 11	0.5116167 ± 2	-12.1	-18.7	-2.7
M19	D	4	R	3	62	63	470.05	0.282438 ± 9	0.5116524 ± 4	-10.8	-17.9	-2.0
M20	D	4	R	3	66	68	470.09	0.282363 ± 12	0.5117652 ± 4	-14.0	-15.8	-6.9
M21	D	4	R	3	76	78	470.19	0.282332 ± 8	0.5117594 ± 5	-14.9	-15.9	-7.7
M22	D	4	R	3	83	85	470.26	0.282255 ± 13	0.5118258 ± 4	-17.8	-14.7	-11.5
M23	D	4	R	3	93	95	470.36	0.282342 ± 7	0.5118490 ± 4	-14.5	-14.2	-8.6
M24	D	4	R	3	96	97	470.39	0.282379 ± 10	0.5118529 ± 3	-13.2	-14.1	-7.4

M25	D	4	R	3	104	106	470.47	0.282230 ± 8	0.5117439 ± 5	-18.2	-16.1	-10.9
M26	D	4	R	3	124	126	470.67	0.282414 ± 11	0.5119031 ± 6	-12.1	-13.2	-7.1
M27	D	4	R	3	135	136	470.77	0.282416 ± 15	0.5118824 ± 5	-12.3	-13.8	-6.8
M28	D	4	R	4	1	3	470.94	0.282470 ± 9	0.5119418 ± 6	-10.9	-12.6	-6.2
M29	D	4	R	4	13	15	471.06	0.282495 ± 14	0.5120234 ± 4	-14.4	-11.0	-11.0
M30	D	4	R	4	37	39	471.30	0.282425 ±6	0.5120126 ± 6	-12.1	-11.1	-8.7
M31	D	4	R	4	61	63	471.54	0.282547 ± 25	0.5119490 ± 7	-7.7	-12.4	-3.2
M32	D	4	R	4	96	98	471.90	0.282540 ± 6	0.5120229 ± 4	-8.1	-11.0	-4.8
M33	D	4	R	5	28	30	472.38	0.282473 ± 16	0.5119455 ± 3	-12.5	-12.5	-8.0
M34	C	32	R	2	140	141	472.85	0.282480 ± 6	0.5119108 ± 5	-11.3	-13.1	-6.2
M35	C	32	R	3	60	61	473.56	0.282484 ± 15	0.5118433 ± 3	-10.4	-14.4	-4.4

5

5. Discussion

5.1 Behaviour of Hf isotopes during reverse weathering

A prerequisite for the use of $\triangle\varepsilon_{Hfclay}$ as a paleoweathering proxy is that the degree of Hf-Nd isotope decoupling in clay-size sediments is not controlled by the presence of unradiogenic zircon nor by any post-depositional processes. While the presence of zircon in clay-size fractions can be assessed using Zr and shale-normalized heavy-REE abundances (see section 5.2), to date, there is little information about the behaviour of Nd and Hf isotopes during diagenesis, especially during *in situ* formation of aluminosilicate minerals, a process referred to as 'reverse weathering' in marine sediments (Michalopoulos and Aller, 1995). During reverse weathering, the combined dissolution of biogenic opal, metal hydroxides and organic matter under anoxic conditions leads to rapid precipitation of authigenic clay minerals (Michalopoulos and Aller, 1995; Wallmann et al., 2008). This process typically results in the preferential incorporation and/or absorption of dissolved cations (e.g., Fe, K, and Mg) from surrounding pore waters into newly formed clay minerals, associated with kinetic isotope effects (e.g., Santiago Ramos et al., 2018). Reverse weathering generally occurs in close association with the dissolution of detrital silicate minerals under anoxic conditions; a process referred to as marine silicate weathering, which can be inferred from anomalously high total alkalinity (TA) levels (>40 mM) in continental margin sediments (Wallmann et al., 2008), or from radiogenic Sr isotopic compositions of pore waters departing from seawater values (e.g., Torres et al., 2020). At Site U1516, present-day alkalinity levels in interstitial waters never exceed ~6.5 mM in the upper, carbonate-dominated, sedimentary column (<440 mbsf), reflecting limited organic matter remineralization rate (Huber et al., 2019). However, during OAE 2, rapid accumulation

of abundant terrigenous material, biogenic opal and organic matter at the seafloor, combined with the onset of anoxic deep-water conditions (Petrizzo et al., 2021; Chen et al., 2022), provided ideal conditions for post-depositional dissolution of silicate minerals coupled with clay authigenesis (reverse weathering). Such intense early diagenetic processes could have led to strong Hf-Nd isotope decoupling in corresponding clay-size fractions, thereby biasing the interpretation of $\triangle\varepsilon_{Hfclay}$ as a paleoproxy for continental chemical weathering.

In this study, the influence of marine silicate weathering and subsequent clay authigenesis on Nd-Hf isotope decoupling has been evaluated using the suite of samples collected from methanogenic sediment layers at continental margins. At present, these sediment samples probably experience the same diagenetic conditions as the sediment deposited at Site U1516 during OAE 2. While both Nd and Hf isotopic compositions of studied clay-size fractions vary from one site to another, reflecting different geological settings and provenance, clay-size fractions at each site display similar $\triangle\varepsilon_{Hfclay}$ values regardless of corresponding TA levels in pore waters (Fig. 2 and Table S1). This observation suggests no measurable influence of reverse weathering on the Hf-Nd isotope compositions of clay-size fractions, despite clear evidence for ongoing marine silicate weathering (TA >40 mM) at all studied sites (Fig. 2 and Table S1). To some extent, the lack of any particular $\triangle\varepsilon_{Hfclay}$ difference between clays recovered from sediment layers having experienced differing degrees of marine silicate and reverse weathering intensity reflects the fact that both Hf and REE are present in very low concentrations in pore waters relative to detrital silicate minerals. In agreement with recent findings suggesting that the REE cycling during clay marine authigenesis is coupled with dissolution of detrital clay

minerals (Abbott et al., 2019), our results suggest that marine silicate weathering under anoxic conditions is possibly followed by quantitative incorporation of released REE and Hf into neoformed authigenic clay minerals during reverse weathering, hence preserving inherited detrital Nd and Hf isotopic signatures. In this context, our new data provide empirical support for the reliability of Hf-Nd isotopes as continental weathering proxies in organic-rich marine sediments experiencing reverse weathering. By analogy, therefore, we infer that during OAE 2, the deposition of organic-rich black shale sediment at Site U1516, presumably associated with the co-occurrence of marine silicate weathering and clay authigenesis in the sub-seafloor environment, had negligible impact on the $\triangle\varepsilon_{Hfclay}$ composition of clay-size detrital minerals.

5.2 Application of Hf isotopes as paleoweathering proxies

In this study, the evolution of continental chemical weathering during OAE 2 is reconstructed using $\triangle\varepsilon_{Hfclay}$ (Bayon et al., 2016) (Fig. 3). The use of this quantitative measure of Hf-Nd isotope decoupling as a weathering proxy is based on the evidence that $\triangle\varepsilon_{Hfclay}$ in modern river clays displays strong relationships with climatic parameters of corresponding river basins (Bayon et al., 2016). Positive $\triangle\varepsilon_{Hfclay}$ values indicate more intense chemical weathering under warm and wet climate conditions, reflecting presumably the recycling of radiogenic apatite and other secondary phosphate-bearing minerals in soils (Banfield and Eggleton, 1989; Bayon et al., 2016). In soils, preferential dissolution of poorly resistant accessory minerals such as allanite and apatite typically leads to formation of secondary phosphate minerals such as florencite and rhabdophane (Banfield and Eggleton, 1989). While being more stable than their corresponding primary minerals, these secondary phases can undergo dissolution under more

intense weathering conditions (Banfield and Eggleton, 1989), presumably releasing a substantial fraction of radiogenic Hf in soils that can be subsequently incorporated into neoformed clay minerals. In contrast, the most negative $\triangle\varepsilon_{Hfclay}$ values in river-borne sediments are typically encountered in subarctic catchments draining crystalline rocks that undergo limited chemical weathering, reflecting the overwhelming presence of primary rock-forming minerals relative to secondary clay mineral assemblages (Bindemann et al., 2019). Nevertheless, particular care shall be taken prior to using $\triangle\varepsilon_{Hfclay}$ as a weathering proxy, because additional factors such as mineral sorting, provenance, or sediment recycling can also potentially influence the Hf isotopic composition of fine-grained siliciclastic sediments (Bayon et al., 2016). Below, we briefly review these potential factors, in order to show that they are unlikely to affect the use of $\triangle\varepsilon Hf_{clay}$ as a paleoweathering proxy at Site U1516.

First, the relatively low Zr abundances (average 67.5 ± 12 µg/g) in clay-size fractions at Site U1516 and the absence of correlation trend between Zr/Rb ratios and ε_{Hf} values (R^2 = 0.08; plot not shown here) both indicate negligible influence of a putative zircon effect. Except for three samples that were discarded (see Supplementary text), the absence of characteristic heavy-REE enrichments in shale-normalized REE patterns also points towards the absence of zircon or any other heavy accessory minerals in studied clay-size fractions (Fig. S1).

In addition to the zircon effect, the presence of mafic rocks in the source regions, which weather faster than other types of rocks, can yield much higher $\triangle\varepsilon_{Hfclay}$ in fine-grained volcanogenic sediments transported by river systems (Bayon et al., 2016; Bayon et al., 2022). In this study, the potential influence of basalt weathering on measured $\triangle\varepsilon_{Hfclay}$ values at Site

U1516 can be excluded due to insignificant contribution of volcanogenic material from the Kerguelen Plateau during OAE 2 (Chen et al., 2022).

Recycling of old sedimentary material derived from former erosional cycles could represent an additional factor complicating the use of $\triangle\varepsilon_{Hfclay}$ or any other weathering proxy in the sedimentary record. However, as discussed in previous studies, the close relationship commonly observed in catchments between modern climatic parameters and the degree of weathering of fine-grained sediments derived from ancient shale formations suggests that the material exported from river systems, at least at passive margins, can still carry useful information on contemporaneous weathering conditions (e.g., Bayon et al., 2018; Dere et al., 2013). Additionally, clay-size detrital sediments at Site U1516 were mainly transported from drainage basins dominated by Precambrian granitoids and gneisses in southwest Australia (e.g., Chen et al., 2022 and references therein), hence further precluding any significant impact of sedimentary recycling in the interpretation of our weathering proxy records.

Concerning the potential influence of sediment provenance, its evolution at Site U1516 across OAE 2 has been recently discussed in detail (Chen et al., 2022), indicating a major change during Phase II of the OAE 2, coinciding with a shift towards more negative ε_{Nd} values. Chen et al. (2022) interpreted this major ε_{Nd} shift as reflecting major drainage reorganization in southwest Australia, associated with enhanced contribution from distant sediment sources (Yilgarn Craton and Albany-Fraser Orogen) relative to proximal regions (Leeuwin Block and Perth Basin) (Figs. 1 and 3). However, in this study, the absence of any significant correlation between $\varepsilon_{Hf(i)}$ and $\varepsilon_{Nd(i)}$ in clay-size fractions ($R^2 = 0.01$, $p < 0.05$), nor of any relationships

between median grain size and $\varepsilon_{Hf(i)}$ (R^2 = 0.02, p <0.05), precludes any major control of sediment provenance on measured $\triangle\varepsilon_{Hfclay}$ values at Site U1516 (Fig. 3).

Therefore, except for a particular sediment interval that will be specifically discussed below (see section 5.3), the observed $\triangle\varepsilon_{Hfclay}$ variability at Site U1516 is probably best explained by changes in chemical weathering intensity, as proposed in previous studies (Bayon et al., 2016; Bayon et al., 2022; Corentin et al., 2022). Interestingly, as illustrated in Fig. 3, conventional indices of chemical weathering such as the chemical index of weathering (CIA) and potassium/aluminum (K/Al) ratios, which are commonly used to track the intensity of feldspar weathering, display no correlation with $\triangle\varepsilon_{Hfclay}$ during Phase II of the OAE 2. In contrast to $\triangle\varepsilon_{Hfclay,}$ we infer that the observed shifts in CIA and K/Al at Site U1516 are mostly caused by changes in sediment provenance associated with enhanced delivery of K-bearing mineral assemblages such as illite during OAE 2 (Chen et al., 2022). This assumption is supported by the strong relationship observed between illite contents and K/Al (R^2 = 0.47, p < 0.05), and evidence that both K/Al and CIA display significant correlation with Nd isotope ratios at Site U1516 ($R^2_{K/Al\ vs.\ \varepsilon Nd}$= 0.42, $R^2_{CIA\ vs.\ \varepsilon Nd}$ = 0.25, p < 0.05) (Fig. 3).

To summarize, none of the potential additional controls on $\triangle\varepsilon_{Hfclay}$ at Site U1516, namely the zircon effect, the presence of volcanogenic sediment, sediment recycling, or provenance change, are likely to explain the observed $\triangle\varepsilon_{Hfclay}$ variability at Site U1516 during OAE 2. Therefore, on the basis of the relationships previously documented between $\triangle\varepsilon_{Hfclay}$ and the degree of chemical weathering intensity in modern river clays, we propose that the $\triangle\varepsilon_{Hfclay}$ shift

towards positive values identified at Site U1516 was induced by intensifying chemical weathering in the source region (southwest Australia).

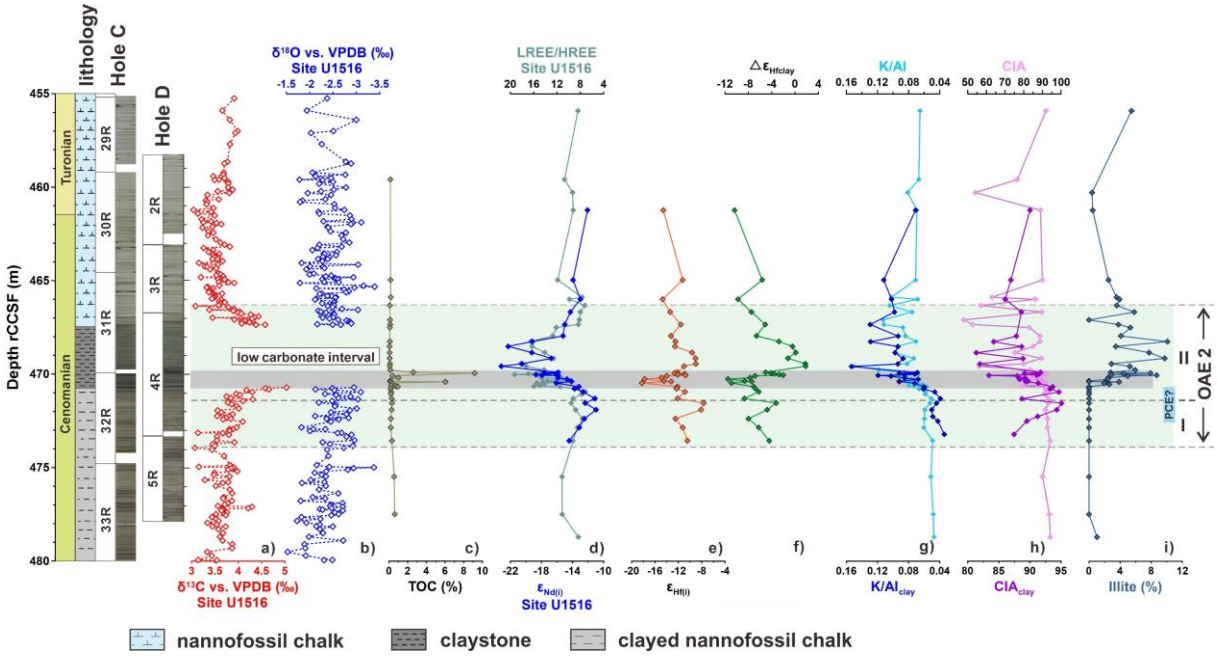

Fig. 3. Stratigraphy, lithology and geochemistry of Site U1516 sediments during the OAE 2 interval. a) $\delta^{13}C$ and b) $\delta^{18}O$ of bulk carbonate (Petrizzo et al., 2021); c) total organic carbon (TOC) contents (Chen et al., 2022); d) ε_{Nd} of clay-size fractions and light-REE/heavy-REE (LREE/HREE) ratio; e) ε_{Hf} of clay-size fractions; f) $\triangle\varepsilon_{Hfclay}$; g) K/Al ratios (in reverse axis); h) CIA; and i) illite content. The light green and grey bands indicate the OAE 2 interval and black shale unit, respectively.

5.3 Sediment flushing following abrupt river reactivation at the onset of Phase II of OAE 2

A striking feature of our results is the abrupt $\triangle\varepsilon_{Hf(i)clay}$ excursion towards highly negative values (-11.5) at the onset of Phase II of the OAE 2, with values even departing from the observed $\triangle\varepsilon_{Hfclay}$ range in modern river sediments (Fig. 4c). As discussed above, neither reverse weathering nor the presence of unradiogenic zircons is likely to explain this shift towards highly

negative $\triangle\varepsilon_{Hfclay}$ values at Site U1516. Very low $\triangle\varepsilon_{Hfclay}$ values in modern river systems are typically encountered in cold and dry environments dominated by physical erosion, where clay-size fractions are mostly composed of primary mineral assemblages (Bayon et al., 2016; Bindeman et al., 2019). By analogy, the highly negative $\triangle\varepsilon_{Hfclay}$ excursion at Site U1516 could hence indicate the presence of subarctic conditions at that time, associated with limited chemical weathering. However, this hypothesis is incompatible with evidence for relatively high atmospheric temperature (>20 °C) and the onset of hydrological cycle during this particular time interval (Chen et al., 2022; Petrizzo et al., 2021). Evidence for global expansion of forests from middle-to-high latitudes during the mid-Cretaceous also precludes this hypothesis (Zhou et al., 2012). Alternatively, more congruent silicate weathering favoring the alteration of highly-resistant zircons could have possibly led to the release of highly unradiogenic Hf to surface environments, subsequently incorporated by secondary clay minerals upon formation in soils. Most likely, the near-absence of kaolinite at Site U1516, a clay mineral typical of very intense chemical weathering, rules out this hypothesis. Instead, we propose that the $\triangle\varepsilon_{Hfclay}$ shift towards highly negative values at Site U1516 indicates the presence of unweathered primary mineral assemblages rapidly flushed from nearby southwest Australia following the reactivation of river systems. At Site U1516, this particular episode immediately post-dates the late stage of Phase I (Fig. 4), characterized by relatively high $\varepsilon_{Nd(i)}$ and Zr/Rb values, indicative of reduced riverine discharge (and hydrological cycle) and enhanced eolian dust deposition, hence suggestive of arid conditions (Chen et al., 2022). At the onset of Phase II of the OAE 2, the pronounced $\varepsilon_{Nd(i)}$ shift towards unradiogenic values indicates markedly increasing contribution of terrigenous sediments from remote regions in southwest

Australia (e.g., Yilgarn Craton; Fig. 1; Chen et al., 2022). This major shift was previously interpreted as reflecting the reactivation of large river systems induced by enhanced hydrological cycle during OAE 2 (Fig. 4; Chen et al., 2022). At that time, the onset of heavy rainfall episodes could have remobilized poorly weathered sediments previously accumulated in inactive drainage systems, possibly from older soil horizons developed under subarctic conditions, or resulted in rapid erosion of unvegetated bare rock surfaces with limited chemical weathering. To some extent, such a scenario echoes with the abrupt reactivation of paleodrainage systems previously documented in arid North Africa during the Quaternary, which repeatedly occurred following short-term latitudinal shifts of monsoonal rainfall (e.g., Blanchet et al., 2021; Skonieczny et al., 2015). During these humid intervals, moderate annual precipitation levels in North Africa (~ <700 mm/yr) were sufficient to trigger markedly increased fluvial discharges at nearby continental margins (Blanchet et al., 2021). In southwest Australia, such flushing flows leading to remobilization of riverbank sediments or ancient soil horizons during OAE 2 could explain the overwhelming presence of primary mineral assemblages in the exported fine-grained sediment load deposited at Site U1516, as inferred from the $\triangle\varepsilon_{Hfclay}$ excursion towards highly negative values (Fig. 4).

5.4 Enhanced weatherability triggered by southward migration of Southern Hemisphere westerlies and global implications

During the OAE 2, the rise of temperature caused by massive emission of greenhouse gases following the emplacement of LIPs and resulting intensification of the global water cycle is thought to have led to globally enhanced chemical weathering (e.g., Jenkyns, 2010), due to the

dependency of silicate mineral dissolution rates to temperature and precipitation. At Site U1516, the major $\triangle\varepsilon_{Hfclay}$ increase from -11.5 to +1.8 during this period is fully consistent with intensifying chemical weathering conditions (Fig. 4). Bulk carbonate $\delta^{18}O$ indicates that sea-surface paleotemperature (SST) at Site U1516 peaked during OAE 2 and remained relatively stable between ~20–23.5°C (Petrizzo et al., 2021), consistent with another SST record at Southern Hemisphere mid-latitudes (ODP Site 1138; Fig. 1; paleolatitude ~47°S) (Robinson et al., 2019). In southwest Australia, the intensification of chemical weathering inferred from $\triangle\varepsilon_{Hfclay}$ coincides with the most prominent CIE at Site U1516, but also with a major $\varepsilon_{Nd(i)}$ shift in clay-size fractions towards unradiogenic values (Fig. 4). As mentioned above, this latter $\varepsilon_{Nd(i)}$ shift has been interpreted as reflecting the onset of intense hydrological cycle in southwest Australia, associated with riverine export of terrigenous material from distant source regions (Fig. 4b). The strong relationship between $\triangle\varepsilon_{Hfclay}$ and $\varepsilon_{Nd(i)}$ during this particular period of the OAE 2 (R^2 = 0.57 during Phase II, p <0.05) suggests that the intensification of chemical weathering was caused by increasing precipitation levels rather than by rising atmospheric temperature changes. By comparing our results to those for modern river clays (Bayon et al., 2016), we infer that the $\triangle\varepsilon_{Hfclay}$ shift towards positive values during phase II of OAE 2 indicates a transition from reduced chemical weathering under arid climate to moderate weathering intensity associated with humid conditions. This observation is coherent with recent paleontological investigations suggesting the development of temperate-warm and humid climate at high latitudes during the mid-Cretaceous (Varela et al., 2018).

Taken together, our combined evidence for enhanced fluvial discharges (inferred from Nd isotopes and clay mineralogy; Chen et al., 2022) and intensifying chemical weathering (inferred

from $\triangle\varepsilon_{Hfclay}$; this study) hence provide direct support for a greater susceptibility of the land surface to chemical erosion (i.e., weatherability) during OAE 2 (Fig. 4). This finding of a greater weatherability at the regional scale of southwest Australia during OAE 2 is consistent with existing δ^7Li and $^{87}Sr/^{86}Sr$ proxy record of global seawater chemistry, which collectively point towards enhanced continental fluxes to the ocean at this period (Pogge von Strandmann et al., 2013; Yobo et al., 2021), despite some discrepancies in the timing of proxy-inferred weathering changes that most likely relate to the regional ($\triangle\varepsilon_{Hfclay}$) versus global (e.g., δ^7Li) significance of studied proxies (Fig. 4).

By extrapolation, our combined Nd-Hf isotope evidence for enhanced rainfall and intensifying chemical weathering in southwest Australia implies the possibility that similar conditions prevailed in other high-latitude regions during OAE 2 (e.g., Gangl et al., 2019). While the hydroclimate evolution of southern high latitudes during OAE 2 remains poorly documented, various climate proxy data and modeling studies have suggested the occurrence of humid conditions at middle-high latitudes during the mid-Cretaceous (Klages et al., 2020; Varela et al., 2018), possibly related to a drastic shrinking of the Hadley circulation and poleward migration of the westerlies (e.g., Hasegawa et al., 2012). Our Nd-Hf isotopic data provide direct support to the above-mentioned studies, further suggesting that the onset of OAE 2 was associated with enhanced hydrological cycle in high-latitude regions. Although the total areal extent of the emerged continental surface decreased during the mid-Cretaceous, due to global transgression, a substantial fraction of continental landmasses was located in middle-high latitude areas during that period (Fig. 1). By inference, the onset of enhanced weatherability during the peak OAE 2 warmth probably resulted in accelerated nutrient releases

to the ocean, promoting high primary productivity at ocean margins surrounding middle-high latitude regions. To summarize, our findings support the view that enhanced weatherability in middle-high latitude regions, associated with the poleward migration of the southern westerlies during the peak OAE 2 warmth, possibly played a key role in atmospheric CO_2 drawdown at that time, through accelerated continental chemical weathering of silicate rocks and organic carbon burial in marine sediments, which altogether could have contributed to the termination of OAE 2. Future studies combining proxy records for chemical weathering at different latitudes and coupled ocean-atmosphere models integrating paleogeographic reconstructions and global carbon cycle will be required to test the reliability of this hypothesis.

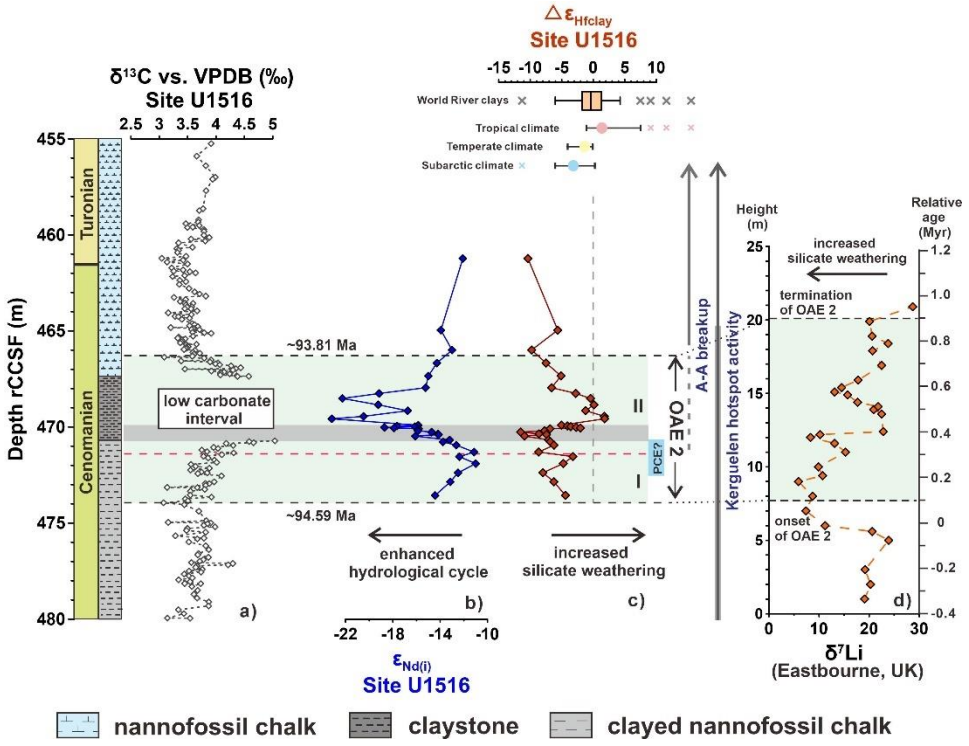

Fig. 4. a) $\delta^{13}C$ of bulk carbonate (Petrizzo et al., 2021), b) $\varepsilon_{Nd(i)}$, and c) $\triangle\varepsilon_{Hfclay}$ at Site U1516 compared with d) $\delta^{7}Li$ records of marine carbonate sections in Eastbourne, UK (Pogge von Strandmann et al., 2013). The global range of $\triangle\varepsilon_{Hfclay}$ in modern river sediments and for different climatic zones (subarctic, temperate, humid) are also shown for comparison (Bayon et

al., 2016). Note that a few outliers for $\triangle\varepsilon_{Hfclay}$ in modern river sediments are indicated as red, yellow, and blue dots, respectively. The light green and grey bands indicate OAE 2 intervals and black shale units, respectively. A-A = Australia-Antarctica.

Concluding remarks

The novel $\triangle\varepsilon_{Hfclay}$ proxy for chemical weathering was applied to a sedimentary sequence from the Mentelle Basin (Site U1516), retrieved during IODP Expedition 369 in order to reconstruct the evolution of continental weathering at southern high latitudes during the Ocean Anoxic Event (OAE 2). Complementary Hf-Nd isotope analyses of a suite of modern methanogenic sediments influenced by marine silicate weathering suggest that $\triangle\varepsilon_{Hfclay}$ is negligibly affected by post-depositional processes such as reverse weathering, and hence can serve as a reliable proxy for chemical weathering during extreme climate events such as OAE 2. At Site U1516, the evolution of $\triangle\varepsilon_{Hfclay}$ provides first direct evidence for a major shift towards markedly enhanced weatherability in southwest Australia during the peak OAE 2 warmth, i.e., the interval characterized by the most prominent CIE. We interpret this result as reflecting the onset of hydrological cycle in southern high latitudes due to the poleward migration of the westerlies, possibly associated with a drastic shrinking of the Hadley circulation at that time. These findings emphasize the important role of chemical weathering in middle-high latitude regions as a potential sink for atmospheric CO_2 during OAE 2, which, together with associated nutrient export to the ocean, primary productivity and organic matter burial in the sea, possibly allowed the recovery of the Earth's climate system from a super-greenhouse state.

Acknowledgment

This research used samples provided by ODP and IODP. This study is financially supported by the National Key Research and Development Program of China (2022YFF0800503), the National Natural Science Foundation of China (41876034), the Strategic Priority Research Program of the Chinese Academy of Sciences (XDB42000000 and XDB40010100), the Marine S&T Fund of Shandong Province for Pilot National Laboratory for Marine Science and Technology (Qingdao; 2022QNLM050203), the National Natural Science Foundation of China (41676038 and 41830539), and Taishan Scholars Project Funding, and a grant to G.B. from the French National Research Agency (ANR-20-CE01-0003). We are most grateful to the Editor (A.D. Jacobson) and two anonymous reviewers for providing insightful and constructive comments. H.C. acknowledges the China Scholarship Council for supporting a research visit at IFREMER. M.-L. Rouget, B. Gueguen and A. Trinquier are thanked for support during elemental and isotopic analyses, respectively.

References

Abbott, A. N., Löhr, S., Trethewy, M., 2019. Are clay minerals the primary control on the oceanic rare earth element budget?. Front. Mar. Sci. 6, 504.

Albarède, F., Simonetti, A., Vervoort, J.D., Blichert-Toft, J., Abouchami, W., 1998. A Hf-Nd isotopic correlation in ferromanganese nodules. Geophys. Res. Lett. 25, 3895-3898.

Arthur, M.A., Schlanger, S.O., Jenkyns, H.C., 1987. The Cenomanian-Turonian Oceanic Anoxic Event, II. Palaeoceanographic controls on organic-matter production and preservation. Geol. Soc. (Lond.) Spec. Publ. 26, 401-420.

Banfield, J. F., Eggleton, R. A., 1989. Apatite replacement and rare earth mobilization, fractionation, and fixation during weathering. Clay Clay Miner. 37, 113-127.

Batenburg, S., Bogus, K., Jones, M., Macleod, K., Martinez, M., 2021. The rhythmic expression of mid-cretaceous Oceanic Anoxic Event 2 at IODP Site U1513 and U1516 (southwest of Australia). In: EGU General Assembly Conference Abs., pp. EGU21-11977.

Bayon, G., Bindeman, I. N., Trinquier, A., Retallack, G. J., Bekker, A., 2022. Long-term evolution of terrestrial weathering and its link to Earth's oxygenation. Earth Planet. Sci. Lett. 584, 117490.

Bayon, G., Burton, K. W., Soulet, G., Vigier, N., Dennielou, B., Etoubleau, J., Ponzevera, E., German, C. R., Nesbitt, R.W., 2009. Hf and Nd isotopes in marine sediments: Constraints on global silicate weathering. Earth Planet. Sci. Lett. 277, 318-326.

Bayon, G., Delvigne, C., Ponzevera, E., Borges, A. V., Darchambeau, F., Deckker, P. D., Lambert, T., Monin, L., Toucanne, S., André, L., 2018. The silicon isotopic composition of fine-grained river sediments and its relation to climate and lithology. Geochim. Cosmochim. Acta 229, 147-161.

Bayon, G., Skonieczny, C., Delvigne, C., Toucanne, S., Bermell, S., Ponzevera, E., André, L., 2016. Environmental Hf–Nd isotopic decoupling in World river clays. Earth Planet. Sci. Lett. 438, 25-36.

Bayon, G., Toucanne, S., Skonieczny, C., André, L., Bermell, S., Cheron, S., Dennielou, B., Etoubleau, J., Freslon, N., Gauchery, T., Germain, Y., Jorry, S. J., Ménot, G., Monin, L., Ponzevera, E., Rouget, M.-L., Tachikawa, K., Barrat, J. A., 2015. Rare Earth elements and neodymium isotopes in World river sediments revisited. Geochim. Cosmochim. Acta 170, 17-38

Bayon, G., Vigier, N., Burton, K.W., Jean Carignan, A.B., Etoubleau, J., Chu, N.C., 2006. The control of weathering processes on riverine and seawater hafnium isotope ratios. Geology 34, 433-436.

Bindeman, I. N., Bayon, G., Palandri, J., 2019. Triple oxygen isotope investigation of fine-grained sediments from major world's rivers: Insights into weathering processes and global fluxes into the hydrosphere. Earth Planet. Sci. Lett. 528, 115851.

Blanchet, C.L., Osborne, A.H., Tjallingii, R. Ehrmann, W., Friedrich, T., Timmermann, A., Brückmann, W., Frank, M., 2021. Drivers of river reactivation in North Africa during the last glacial cycle. Nat. Geosci. 14, 97-103.

Blättler, C.L., Jenkyns, H.C., Reynard, L.M., Henderson, G.M., 2011. Significant increases in global weathering during Oceanic Anoxic Events 1a and 2 indicated by calcium isotopes. Earth Planet. Sci. Lett. 309, 77-88.

Bottini, C., Cohen, A.S., Erba, E., Jenkyns, H.C., Coe, A.L., 2012. Osmium-isotope evidence for volcanism, weathering, and ocean mixing during the early Aptian OAE 1a. Geology 40, 583-586.

Boulila, S., Charbonnier, G., Spangenberg, J.E., Gardin, S., Galbrun, B., Briard, J., Callonnec, L.L., 2020. Unraveling short- and long-term carbon cycle varations during the Oceanic Anoxic Event 2 from the Paris Basin Chalk. Glob. Planet. Change 186, 103126.

Bouvier, A., Vervoort, J.D., Patchett, P.J., 2008. The Lu–Hf and Sm–Nd isotopic composition of CHUR: Constraints from unequilibrated chondrites and implications for the bulk composition of terrestrial planets. Earth Planet. Sci. Lett. 273, 48-57.

Chen, H., Xu, Z., Bayon, G., Lim, D., Batenburg, S.J., Petrizzo, M.R., Hasegawa, T., Li, T., 2022. Enhanced hydrological cycle during Oceanic Anoxic Event 2 at southern high latitudes: New insights from IODP Site U1516. Glob. Planet. Change 209, 103735.

Corentin, P., Pucéat, E., Pellenard, P., Freslon, N., Guiraud, M., Blondet, J., Adatte, T., Bayon, G., 2022. Hafnium-neodymium isotope evidence for enhanced weathering and uplift-climate interactions during the Late Cretaceous. Chem. Geol. 591, 120724.

Dere, A.L., White, T.S., April, R.H., Reynolds, B., Miller, T.E., Knapp, E.P., McKay, L.D., Brantley, S.L., 2013. Climate dependence of feldspar weathering in shale soils along a latitudinal gradient. Geochim. Cosmochim. Acta 122, 101–126.

Dickson, A.J., Saker-Clark M., Jenkyns, H.C., Bottini, C., Erba, E., Russo, F., Gorbaneko, O., Naafs, B.D.A., Pancost, R.D., Robinson, S.A., van den Boorn, S.H.J.M., Idiz, E., 2017. A Southern Hemisphere record of global trace-metal drawdown and orbital modulation of organic-matter burial across the Cenomanian–Turonian boundary (Ocean Drilling Program Site 1138, Kerguelen Plateau). Sedimentology 64, 186-203.

Du Vivier, A. D., Jacobson, A. D., Lehn, G. O., Selby, D., Hurtgen, M. T., Sageman, B. B., 2015. Ca isotope stratigraphy across the Cenomanian–Turonian OAE 2: Links between volcanism, seawater geochemistry, and the carbonate fractionation factor. Earth Planet. Sci. Lett. 416, 121-131.

Frijia, G., Parente, M., 2008. Strontium isotope stratigraphy in the upper Cenomanian shallow-water carbonates of the southern Apennines: Short-term perturbations of marine $^{87}Sr/^{86}Sr$ during the Oceanic Anoxic Event 2. Palaeogeogr. Palaeoclimatol. Palaeoecol. 261, 15-29.

Gangl, S.K., Moy, C.M., Stirling, C.H., Jenkyns, H.C., Crampton, J.S., Clarkson, M.O., Ohneiser, C., Porcelli, D., 2019. High-resolution records of Oceanic Anoxic Event 2: insights into the timing, duration and extent of environmental perturbations from the palaeo-South Pacific Ocean. Earth Planet. Sci. Lett. 518, 172-182.

Garçon, M., Chauvel, C., France-Lanord, C., Huyghe, P., Lavé, J., 2013. Continental sedimentary processes decouple Nd and Hf isotopes. Geochim. Cosmochim. Acta. 121, 177-195.

Hasegawa, H., Tada, R., Jiang, X., Suganuma, Y., Imsamut, S., Charusiri, P., Ichinnorov, N., Khand, Y., 2012. Drastic shrinking of the Hadley circulation during the mid-Cretaceous Supergreenhouse. Clim. Past. 8, 1323-1337.

Huber, B.T., Hobbs, R.W., Bogus, K.A., and the Expedition 369 Scientists, 2019. Expedition 369 summary. Proceedings of the International Ocean Discovery Program, 369.

Huber, B.T., MacLeod, K.G., Watkins, D.K., Coffin, M.F., 2018. The rise and fall of the Cretaceous Hot Greenhouse climate. Glob. Planet. Change 167, 1-23.

Jenkyns, H.C., 2010. Geochemistry of oceanic anoxic events. Geochem. Geophy. Geosy. 11, 1-30.

Kump, L. R, Brantley, S. L., Arthur, M. A., 2000. Chemical weathering, atmospheric CO_2, and climate. Annu. Rev. Earth Planet. Sci. 28, 611-667.

Macdonald, F. A., Swanson-Hysell N. L., Park, Y., Lisiecki, L., Jagoutz, O., 2019. Arc-continent collisions in the tropics set Earth's climate state. Science, 364, 181-184.

Michalopoulos, P., Aller, R.C., 1995. Rapid Clay Mineral Formation in Amazon Delta Sediments: Reverse Weathering and Oceanic Elemental Cycles. Science 270, 612-617.

Mill, B., Lenton, T.M., Watson, A.J., 2014. Proterozoic oxygen rise linked to shifting balance between seafloor and terrestrial weathering. Proc. Natl. Acad. Sci.111, 9073-9078.

Misra, S., Froelich, P. N., 2012. Lithium isotope history of Cenozoic seawater: changes in silicate weathering and reverse weathering. Science 335, 818-823.

O'Brien, C.L., Robinson, S.A., Pancost, R.D., Sinninghe Damsté, J.S., Schouten, S., Lunt, D.J., Alsenz, H., Bornemann, A., Bottini, C., Brassell, S.C., Farnsworth, A., Forster, A., Huber, B.T., Inglis, G.N., Jenkyns, H.C., Linnert, C., Littler, K., Markwick, P., McAnena, A., Mutterlose, J., Naafs, B.D.A., Püttmann, W., Sluijs, A., van Helmond, N.A.G.M., Vellekoop, J., Wagner, T., Wrobel, N.E., 2017. Cretaceous sea-surface temperature evolution: Constraints from TEX_{86} and planktonic foraminiferal oxygen isotopes. Earth Sci. Rev. 172, 224-247.

O'Connor, L. K., Jenkyns, H. C., Robinson, S. A., Remmelzwaal, S. R., Batenburg, S. J., Parkinson, I. J., Gale, A. S., 2020. A re-evaluation of the Plenus Cold Event, and the links between CO_2, temperature, and seawater chemistry during OAE 2. Paleoceanogr. Paleoclimatol. 35, e2019PA003631.

Penman, D.E., Rugenstein, J.K.C., Ibarra, D.E., Winnick, M.J., 2020. Silicate weathering as a feedback and forcing in Earth's climate and carbon cycle. Earth-Sci. Rev. 209, 103298.

Petrizzo, M.R., Watkins, D.K., MacLeod, K.G., Hasegawa, T., Huber, B.T., Batenburg, S.J., Kato, T., 2021. Exploring the paleoceanographic changes registered by planktonic foraminifera across the Cenomanian-Turonian boundary interval and Oceanic Anoxic Event 2 at southern high latitudes in the Mentelle Basin (SE Indian Ocean). Glob. Planet. Change 206, 103595.

Pogge von Strandmann, P.A.E., Jenkyns, H.C., Woodfine, R.G., 2013. Lithium isotope evidence for enhanced weathering during Oceanic Anoxic Event 2. Nat. Geosci. 6, 668-672.

Rickli, J., Frank, M., Stichel, T., Georg, R.B., Vance, D., Halliday, A.N., 2013. Controls on the incongruent release of hafnium during weathering of metamorphic and sedimentary catchments. Geochim. Cosmochim. Acta 101, 263-284.

Robinson, S.A., Dickson, A.J., Pain, A., Jenkyns, H.C., O'Brien, C.L., Farnsworth, A., Lunt, D.J., 2019. Southern Hemisphere sea-surface temperatures during the Cenomanian–Turonian: Implications for the termination of Oceanic Anoxic Event 2. Geology 47, 131-134.

Santiago Ramos, D.P., Morgan, L.E., Lloyd, N.S., Higgins, J.A., 2018. Reverse weathering in marine sediments and the geochemical cycle of potassium in seawater: Insights from the K isotopic composition ($^{41}K/^{39}K$) of deep-sea pore-fluids. Geochim. Cosmochim. Acta 236, 99-120.

Schlanger, S.O., Jenkyns, H.C., 1976. Cretaceous oceanic anoxic events: causes and consequences. Geologie en mijnbouw 55, 179-184.

Skonieczny, C., Paillou, P., Bory, A., Bayon, G., Biscara, L., Crosta, X., Eynaud, F., Revel, M., Aleman, N., Barusseau, J. -P., Vernet, R., Lopez, S., Grousset, F., 2015. African humid periods triggered the reactivation of a large river system in Western Sahara. Nat. Commun. 6, 1-6.

Takashima, R., Nishi, H., Huber, B., Leckie, R.M., 2006. Greenhouse World and the Mesozoic Ocean. Oceanography 19, 82-92.

Torres, M. E., Hong, W. L., Solomon, E. A., Milliken, K., Kim, J. H., Sample, J. C., Teichert, B. M. A., Wallmann, K., 2020. Silicate weathering in anoxic marine sediment as a requirement for authigenic carbonate burial. Earth Sci. Rev. 200, 102960.

Tsikos, H., Jenkyns, H.C., Walsworth-Bell, B., Petrizzo, M.R., Forster, A., Kolonic, S., Erba, E., Silva, I.P., Baas, M., Wagner, T., Sinninghe, J.S., 2004. Carbon-isotope stratigraphy recorded by the Cenomanian–Turonian Oceanic Anoxic Event: correlation and implications based on three key localities. J. Geol. Soc. 162, 571-576.

Turgeon, S.C., Creaser, R.A., 2008. Cretaceous oceanic anoxic event 2 triggered by a massive magmatic episode. Nature 454, 323-326.

van Helmond, N.A.G.M., Sluijs, A., Reichart, G.J., Sinninghe Damste, J.S., Slomp, C.P., Brinkhuis, H., 2013. A perturbed hydrological cycle during Oceanic Anoxic Event 2. Geology 42, 123-126.

Varela, A.N., Raigemborn, M.S., Richiano, S., White, T., Poiré, D.G., Lizzoli, S., 2018. Late Cretaceous paleosols as paleoclimate proxies of high-latitude Southern Hemisphere: Mata Amarilla Formation, Patagonia, Argentina. Sediment. Geol. 363, 83-95.

Vervoort, J.D., Plank, T., Prytulak, J., 2011. The Hf–Nd isotopic composition of marine sediments. Geochim. Cosmochim. Acta 75, 5903-5926.

Wallmann, K., Aloisi, G., Haeckel, M., Tishchenko, P., Pavlova, G., Greinert, J., Kutterolf, S., Eisenhauer, A., 2008. Silicate weathering in anoxic marine sediments. Geochim. Cosmochim. Acta 72, 2895-2918.

Yobo, N.L., Brandon, A.D., Holmden, C., Lau, K.V., Eldrett, J., 2021. Changing inputs of continental and submarine weathering sources of Sr to the oceans during OAE 2. Geochim. Cosmochim. Acta 303, 205-222.

Zhao, W., Sun, Y., Balsam, W., Lu, H., Liu, L., Chen, J., Ji, J., 2014. Hf-Nd isotopic variability in mineral dust from Chinese and Mongolian deserts: implications for sources and dispersal. Sci. Rep. 4, 5837, doi.org/10.1038/srep05837.

Zhou, J., Poulsen, C.J., Rosenbloom, N., Shields, C., Briegleb, B., 2012. Vegetation-climate interactions in the warm mid-Cretaceous. Clim. Past 8, 565-576.